minerals

MDPI

Article

Porosity, Mineralogy, Strength, and Reducibility of Sinter Analogues from the Fe_2O_3 (Fe_3O_4)-CaO-SiO_2 (FCS) Ternary System

Isis R. Ignácio [1,*], Geoffrey Brooks [1], Mark I. Pownceby [2], M. Akbar Rhamdhani [1], Willian John Rankin [1,2] and Nathan A. S. Webster [2]

[1] Department of Mechanical and Product Design Engineering, Swinburne University of Technology, John Street, Hawthorn, Melbourne, VIC 3122, Australia
[2] CSIRO Mineral Resources, Private Bag 10, Clayton South, VIC 3169, Australia
* Correspondence: irosaignacio@swin.edu.au

Abstract: The presence of Ca-ferrite and silico-ferrite-of-calcium-and-aluminium (SFCA) bonding phases is thought to be crucial to maintain sinter quality due to their high reducibility and strength levels. However, new evidence suggests that porosity might be an equally important factor controlling reducibility, in addition to mineralogy. This work aims to fundamentally understand the development of porosity in simple sinter analogues from the Fe_2O_3-(Fe_3O_4)-CaO-SiO_2 (FCS) ternary system (with no SFCA), and to connect results back to overall sinter mineralogy, strength, and reducibility properties. Laboratory-scale experiments were conducted to simulate the sintering process by firing tablets of magnetite, hematite, lime and silica mixtures under tightly controlled temperature, holding time and atmosphere conditions. Mineralogy of the fired samples was observed using microscopy techniques, porosity was measured by Mercury Intrusion Porosimetry (MIP), strength was determined using laboratory-scale tumble index equipment and reducibility was measured by the weight loss obtained after reaction of the tablets in a reducing atmosphere of CO/N_2. The results confirmed that reducibility is strongly influenced by porosity, and highly reducible sinters can be produced without forming SFCA-like phases. Magnetite-containing samples had similar reducibility to hematite-containing samples, suggesting that magnetite-based sinters could potentially be used in the blast furnace.

Keywords: iron ore sinter; porosity; reducibility; mineralogy; FCS; strength

check for updates

Citation: Ignácio, I.R.; Brooks, G.; Pownceby, M.I.; Rhamdhani, M.A.; Rankin, W.J.; Webster, N.A.S. Porosity, Mineralogy, Strength, and Reducibility of Sinter Analogues from the Fe_2O_3 (Fe_3O_4)-CaO-SiO_2 (FCS) Ternary System. *Minerals* **2022**, *12*, 1253. https://doi.org/10.3390/min12101253

Academic Editor: Rajesh Kumar Jyothi

Received: 6 September 2022
Accepted: 27 September 2022
Published: 30 September 2022

Publisher's Note: MDPI stays neutral with regard to jurisdictional claims in published maps and institutional affiliations.

Copyright: © 2022 by the authors. Licensee MDPI, Basel, Switzerland. This article is an open access article distributed under the terms and conditions of the Creative Commons Attribution (CC BY) license (https://creativecommons.org/licenses/by/4.0/).

1. Introduction

Iron ore sinter is the main raw material feed to the blast furnace (BF), which is still the primary method for producing pig iron worldwide [1]. Sintering technology was developed to reuse ironmaking residues and to agglomerate ore fines, making them suitable for use in the BF. Iron ore sinter is the result of a complex physico-chemical reaction among the minerals present in the sinter mix in the sintering zone of heating and cooling. The precipitated mineral phases are influenced by maximum temperature reached, chemical composition, oxygen partial pressure (p_{O2}), and cooling rate [2]. The major mineral phases present in fluxed sinters are hematite, calcium ferrites, magnetite, and mixed calcium iron silicates, each of them individually having its own level of reducibility and mechanical properties. Hematite, for instance, is the most reducible among the sinter phases, followed by the Ca-ferrite and SFCA (Silico-ferrite of Calcium and Aluminium) phases, magnetite, and fayalite [3,4].

The biggest advantage of sinter as ferrous burden is that it can be tailor-made. For decades, sinter has been studied to understand its properties in order to increase the efficiency and productivity of the sinter feed to the blast furnace. Much is known therefore about sinter mineralogy and morphology; however, the change in iron ore feed materials

over time, from hematite ores to goethite ores, for example, and the consequent decline in iron ore grades, have led to research in all aspects of the mineralogy and morphology of iron ore sinter.

Ideally, high-quality sinter must be physically strong, easily reduced (i.e., high permeability allowing the passing of reduction gases) and chemically compatible with the requirements of BF chemistry. Pownceby and Clout [4] described an ideal sinter as being composed of a nuclei of unreacted hematite particles (approximately 30%) within a porous bonding matrix (about 70%) formed mainly by the complex SFCA Ca-ferrite-like phases. This mineralogic and textural combination is beneficial for producing optimum levels of reducibility and strength [4,5]. SFCA-I is the most desirable bonding phase in sinter since its microstructure presents higher reducibility and strength compared to SFCA [4], however it is rarely seen in industrial sinters. The SFCA phase is able to maintain a high level of fine porosity during high-temperature reduction [6]. While the chemistry and mineralogy of the product sinter are essential, the pore structure is also a critical parameter that influences sinter quality and productivity. Porosity influences sinter strength (i.e., the formation of large pores or an increase in total porosity [7] may promote breakage), gas permeability (i.e., which depends on the size and connectivity of pores), and stability of the sinter during reduction. It is also known that morphological parameters such as pore size distribution, pore shape, and the proportion of open and closed pores can drastically affect the reducibility and strength of sinter [8]. However, despite many years of research, it is still unclear which factors directly influence porosity and its formation during sintering.

Recent studies on the pore structure and mineralogy of sinter have provided surprising results, raising the question whether sinter structure properties can overcome mineralogy when trying to obtain a good sinter. Harvey et al. 2019 [5], for example, conducted experiments involving firing compact sinter analogues made from hematite ore (−1 mm in size) and fine (−5 µm) chemical reagent/fluxes ($CaCO_3$, $MgCO_3$ and SiO_2), in a controlled gas atmosphere (N_2 and O_2, with $p_{O2} = 5 \times 10^{-3}$), inside an infrared rapid heating furnace, under different temperatures, holding times and cooling rates. Reducibility (through Thermogravimetric Analysis) and porosity (through Mercury Intrusion and Nitrogen Pycnometry) tests were conducted on the fired samples. Results showed that the degree of reduction after 60 min (R_{60}) of samples fired at T_{max} = 1250 °C and 1320 °C did not change significantly compared to the changes in the mineralogy. In other words, reducibility appeared to be insensitive to the mineralogy, suggesting that structure may have more influence on reducibility than mineralogy.

Another recent study by Purohit et al. [9] investigated new alternative processing routes for magnetite ores and identified that a very reducible $CaFe_3O_5$ (CWF) phase could be formed under controlled conditions. In that study, lime magnetite pellets (LMPs) made from synthetic magnetite (Fe_3O_4), $CaCO_3$, and SiO_2 mixtures at different compositions were fired in a horizontal tube resistance furnace under a mildly reducing p_{O2} atmosphere at 850, 950 and 1050 °C, for a wide range of heating times (5 to 720 min). Conditions were designed to maximise the formation of the CWF phase. Scaled-down reducibility test showed that the fired LMPs presented reducibilities that were similar to conventional industrial sinters.

However, while many aspects of iron ore sinter properties have been studied on an individual basis, the complex interplay between reducibility, mineralogy, porosity and strength are still not clear, and an integrated fundamental research study approach is proposed here to contribute to the knowledge of iron ore sinter quality. The current study investigated the phase relations in the Fe_2O_3-(Fe_3O_4)-CaO-SiO_2 (FCS) ternary system to help to build the blocks of knowledge needed for more complex systems. While SFCA is the common phase in industrial sinters due to the presence of alumina as a contaminant in the original ores, there exists an alumina-free analogue of SFCA, known as SFC, which has the same crystal structure [10,11]. The aim was to understand how the texture of sinter analogues without SFCA affects the final sinter properties. Laboratory-scale sintering experiments were conducted at high temperatures in a horizontal tube furnace, where

composition, temperature, holding time, cooling rate, p_{O2}, and flow rate were controlled, and their influence on pore formation and mineralogy were evaluated.

2. Materials and Methods

2.1. Sinter Analogues

Sinter analogues were obtained by combining high-purity synthetic powdered oxides, since their composition is closely controlled and easily reproduced. In real sintering, the sinter feed is formed by larger particles (<6.3 mm) of iron ore which are covered by finer particles of Fe_2O_3, $CaCO_3$, gangue and coke, forming an adhesive layer [12]. Therefore, the size range of the oxides used in this work were selected to correspond to the adhesive layer and to simulate the reactions of real sintering. Fe_3O_4 (<5 μm), Fe_2O_3 (<5 μm), CaO (<0.16 μm), and SiO_2 (<0.014 μm) were mixed in three different ways: pure iron oxides; iron oxides plus lime; and iron oxides plus lime and silica. The basicity (weight ratio of CaO and SiO_2) was kept constant at 2.0, which is the typical basicity used in iron ore sinters [13]. Table 1 shows the compositions of the sinter tablets.

Table 1. Composition of sinter tablets used in the current study (wt%).

Tablet ˆ	Fe_2O_3	Fe_3O_4	CaO	SiO_2	Basicity *
H	100				
M		100			
HL	95.0		5		
ML		95.0	5		
HLS	85		10	5	2.0
MLS		85.0	10	5	2.0

ˆ H = hematite, M = magnetite, HL = hematite + lime, ML = magnetite + lime, HLS = hematite + lime + silica and MLS = magnetite + lime + silica, * Basicity = CaO/SiO_2.

The chemicals were weighed and mixed manually in a mortar and pestle under acetone for homogenization. The amount of acetone used was enough to form a slurry to ensure the non-segregation of material. This slurry was then dried in an oven for 1 h at 110 °C and the mixing process was repeated. The dry powder blends were then pressed in a hydraulic press into 2.5 g (±0.05 g) tablets, using a stainless-steel die with 13 mm diameter. A constant compaction pressure of 4 tonnes was applied for 2 min for all the samples.

2.2. Apparatus and Sintering Conditions

A horizontal tube resistance furnace (RHTH 120-300/18, Nabertherm GmbH, Lilienthal, Germany) with a molybdenum disilicide heating element was used to simulate the industrial sintering process. The furnace was pre-heated to the desired maximum temperature for each experiment, respecting the heating rate of 200 °C/h. A sacrificial alumina tube was placed inside the furnace to protect the main tube during operation and the end flanges were cooled by circulated water. Careful calibration of the furnace was carried out to ensure the exact position and temperature profile of the hot zone.

Duplicate samples were fired simultaneously to ensure that they were exposed to the same conditions inside the hot zone. An alumina rod with an alumina boat attached to the end was used as a sample holder. A piece of nickel foil (99.96% Ni) was placed in the base of the boat, which prevented the sample from reacting with the crucible during heating, thereby increasing its life and preventing alumina contamination of the sintered pellet. The foil was replaced every ten runs. Figure 1 shows the schematic of the furnace set-up.

The compacted tablets were fired under a controlled atmosphere, held for a specific time (t_{hold}) under high temperature (T_{max}), and rapidly cooled by removing the samples from the hot zone and allowing them to cool for two minutes inside the water-cooled flange, simulating the conditions of the flame front in actual sintering. Table 2 shows the

firing conditions adopted and how the samples were identified. The temperatures, holding times and cooling techniques were based on what is observed in industrial sintering and in previous laboratory studies [14].

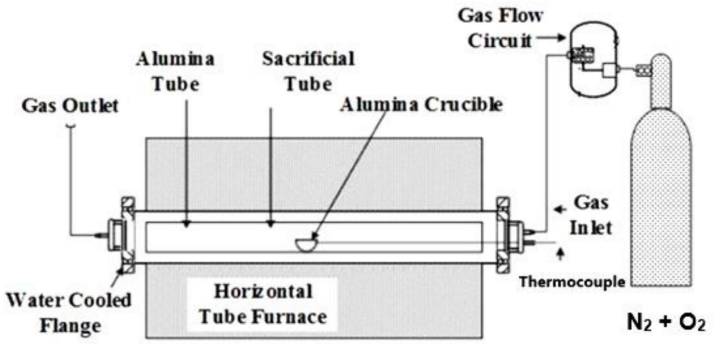


Figure 1. Schematic representation of the horizontal furnace set-up. Adapted from Purohit (2019) [9].

Table 2. Sample identification scheme according to experimental conditions.

Sample No. ˆ	T_{max} (°C)	t_{hold} (min)
XXX 001	1350	4
XXX 002	1300	4
XXX 003	1250	4
XXX 004	1300	2
XXX 005	1300	6

ˆ XXX refers to different tablets identification of H, HL, HLS, M, ML, and MLS, e.g., H001, HL001, HLS001, etc., as given in Table 1.

A pre-mixed gas mixture containing N_2-0.5% O_2, equivalent oxygen partial pressure of $p_{O2} = 5 \times 10^{-3}$ atm was used [4,15,16]. This p_{O2} value is generally chosen for laboratory studies because it generates mineral assemblages and microstructures close to those observed in industrial iron ore sinters [14]. The mixed gas was injected into the furnace at a flow rate of 100 L/h.

A total of 30 samples were sintered, with each sample composition being run in quadruplicate to provide enough material for subsequent analysis. Two pellets were used for strength measurements. As this is a destructive test, the broken pieces were used for mineralogy characterisation tests. One pellet was used for post-heating porosity measurements, and the remaining pellet was used for the reducibility test.

2.3. Characterisation Techniques

X-ray powder diffraction analysis (XRD) was used to identify and quantify the mineral phases which formed. For the analyses, the samples were micronized in ethanol and then dried at 60 °C. After remixing in a mortar and pestle they were backpressed into PANalytical sample holders for flat plate presentation to the X-ray beam. During data collection they were rotated at 60 rpm to improve particle statistics. XRD patterns were collected with a PANalytical X'Pert Pro Multi-purpose Diffractometer (Malvern Panalytical Ltd., Malvern, UK) using Fe filtered Co Ka radiation, an automatic divergence slit, a 2° anti-scatter slit and a fast X'Celerator Si strip detector. Patterns were collected from 4 to 80° in steps of 0.017° 2θ with a counting time of 0.5 s per step, for an overall counting time of approximately 35 min. Phase identification was performed using PANalytical Highscore Plus© software V4.8 (Malvern Panalytical Ltd., Malvern, UK), which interfaces with the International Centre for Diffraction Data (ICDD) PDF 4+ 2021 database. A quantitative phase analysis (QPA) was carried out via the Rietveld method using TOPAS V6 (Bruker AXS, Madison, WI, USA). The internal standard method was used for calculation of amorphous/unidentified phase content using highly crystalline corundum as the standard.

The morphology of the samples was observed using optical microscopy (OM) and scanning electron microscopy (SEM). The sinter samples were prepared by roughly crushing the tablets, mounting a chip in epoxy resin, and then grinding and polishing them to an optically flat, mirrored finish. OM was carried out by placing the polished samples in a moving motorized stepping stage fixed onto an optical microscope (Olympus BX61, Olympus, Tokyo, Japan). Photomicrographs were obtained using a high-resolution camera, allowing clear images of the cross-sectional surface of the sample at different magnifications. For SEM analysis, the same samples were coated with a thin layer (10 nm) of carbon (to prevent electrostatic charging of the surface and to promote a homogeneous emission of secondary electrons). The samples were imaged using a FEI Quanta ESEM (FEI Company, Hillsboro, OR, USA) operating at high vacuum, a working distance of 10 mm, a high voltage of 15 kV, an emission current of 158 μA, a pressure of 1.1×10^{-6} Torr, and a gun pressure of 9.1×10^{-10} Torr. Back Scattered Electron (BSE) photomicrographs were taken at different magnification.

2.4. Strength

Strength was determined using laboratory-scale tumble index (TI) equipment. The same technique was used in previous studies [17–20] and consists of tumbling fired sinter tablets in pairs for 8 min in a modified Bond Abrasion Tester. After tumbling, the material was sieved, and the relative compact TI is given as a percentage of the material retained at above 2 mm. A TI of 80% is considered equivalent to a TI of 65% in a sinter pot-grate test [17].

2.5. Reducibility

Reducibility was measured using a scaled-down technique due to the reduced size of the samples. A thermogravimetric analysis (TGA) set-up was used, consisting of a vertical tube furnace with a control system, and a precision balance (FX-300i with 1 mg accuracy) was placed at the top of the furnace to measure the weight loss of the sample during the reaction. The set-up was previously described by Purohit et al. [21]. A sintered sample, weighting 2.4 g (±0.05 g), was placed inside an alumina crucible held by a platinum wire basket and placed in the hot zone of the furnace. The furnace was sealed, and argon gas was purged to maintain a neutral atmosphere before and after each run. After a few minutes, the reducing atmosphere was created by injecting a mixture of CO/N_2 (40% and 60%, respectively). The temperature for all tests was kept constant at 950 °C, following the ISO 7215:2015 standard [22]. The weight loss was recorded continuously every 0.125 s using WinCT software (A&D, Tokyo, Japan) for 150 min.

2.6. Porosity

Porosity was measured by mercury intrusion porosimetry (MIP). In this method, the sample is immersed in liquid mercury and pressure is applied, forcing the mercury into the pores of the sample. The pressure applied determines total volume and the pore size distribution in the meso- and macro-pore range [23]. A Micrometrics® AutoPore IV (Micromeritics Instrument Corporation, Norcross, GA, USA) was used with pressure ranging from 0 to 60,000 psi, which correlates to the measurement of pores from about 250 μm to 0.003 μm. This work uses the IUPAC classification for pore sizes: micro-pores (radius < 0.002 μm), meso-pores (0.002 μm < radius < 0.05 μm) and macro-pores (radius > 0.05 μm) [23–25].

3. Results

3.1. Mineral Phases and Microstructure in Sinter Analogues

The equilibrium phase relations in the Fe-rich portion of the Fe_2O_3-(Fe_3O_4)-CaO- SiO_2 (FCS) ternary system had been widely studied in the literature [4,26–29], and show the formation process of the silico-ferrite of calcium (SFC), a significant crystalline phase in the system and an important bonding phase in the iron ore sinter [29]. The three most observed

phases in the FCS system are $Ca_2Fe_2O_5$ (C2F), $CaFe_2O_4$ (CF) [30] and $CaFe_4O_7$ (CF2), with CF being stable at temperatures of 1155 to 1226 °C [12]. However, depending on the partial pressure of oxygen, temperature and chemical composition, more of the complex phases $Ca_2Fe_{16}O_{25}$, α-CFF [31], β-CFF [32] and γ-CFF [33] may also be formed.

Table 3 shows the concentration (wt%) of the phases identified in the pre-reduction sinter analogue samples produced in these experiments. Hematite, magnetite, two types of calcium ferrites, γ-CFF ($Ca_3Fe_{14.82}O_{25}$) and CF ($CaFe_2O_4$), and dicalcium silicate (Ca_2SiO_4), also known as larnite, were identified. β-CFF was also identified in the samples containing higher amounts of γ-CFF, HL001 (3%) and HL005 (10%). In the other samples containing γ-CFF, β-CFF was present at less than 1%. Other phases, such as silica (glass), $CaSiO_3$ (wollastonite), cristobalite (high temperature polymorph of SiO_2), $CaFe_2O_5$ (C2F) and maghemite, were also identified in very low concentrations in some samples.

Table 3. Crystalline phase concentration (relative wt%) for the pre-reduction sinter analogues.

Samples	Crystalline Phase Concentration (Relative wt%)					
	Hematite	**Magnetite**	**γ-CFF**	**β-CFF**	**$CaFe_2O_4$**	**Ca_2SiO_4**
H001	96	4				
H002	95	5				
H003	95	4				
H004	96	4				
H005	96	4				
HL001	59		37	3		
HL002	65		33	<1	2	
HL003	59		18	<1	23	
HL004	80	2	6	<1	12	
HL005	33		57	10		
HLS001	75	9	3	<1		11
HLS002	60		30	<1	3	5
HLS003	66	5	12	<1	9	6
HLS004	78	1	6	<1	8	3
HLS005	74	7	6	<1		12
M001	34	66				
M002	41	59				
M003	43	53				
M004	50	45				
M005	32	68				
ML001	7	61	32	<1		
ML002	9	60	31	<1		
ML003	9	60	31	<1		
ML004	12	63	25	<1		
ML005	3	64	33	<1		
MLS001	11	75	3	<1		9
MLS002	16	67	5	<1		9
MLS003	21	61	6	<1		10
MLS004	15	66	5	<1	4	8
MLS005	10	77	4	<1		8

The pure hematite samples (H001-H005) maintained almost constant concentration of hematite (~96%) and magnetite (~4%) under the different sintering conditions. Magnetite formation was not expected here since the gas conditions were not reducing enough to promote magnetite phase formation. It is likely that this represents residual sample contamination. In the pure magnetite samples (M001-M005), magnetite was transformed into hematite (32 to 50%). At the p_{O2} of the experiments this transformation is to be expected as the conditions are in the hematite stability field. It was noted that under the p_{O2} conditions (for the same run time of 4 min), more hematite was present in the

lower temperature experiment (1250 °C) while the higher temperature experiments, being closer to the magnetite-hematite phase transition boundary, maintained a higher level of magnetite. Longer run times (at the same temperature) generated less hematite formation.

As expected, the calcium ferrite phases were formed after lime was added to the mix. For the HL samples, γ-CFF formation was significantly affected by temperature, forming 18% at 1250 °C (HL003) and increasing to 40% at 1350 °C (HL001). Similarly, when holding times were increased from 2 to 6 min, the amount of γ-CFF increased considerably, from 6 to 67% (HL004 and HL005). This indicates that the amount of calcium ferrites formed was mostly affected by the sintering conditions rather than the basicity (when silica was added). This relation was also observed by Murakami et al. [34]. The CF phase was not observed in samples HL001 and HL005, which suggests that CF was totally converted to γ-CFF, or not even formed, at higher temperatures and holding times. However, the same trend was not observed for the ML samples, where temperature and holding time barely affected the proportion of γ-CFF formation, which was between 25 and 33%. No CF was formed in these samples.

When silica was added to the mix (HLS samples), larnite phase was formed and the γ-CFF formation trend noted above was completely different. There was higher formation of larnite at higher temperatures (HLS001) and higher holding times (HLS005), with 11 and 12%, respectively. Silica also appeared to stabilise the formation of the hematite phase for most of the samples, increasing from 33% (HL005) to 78% (HLS004) for the hematite-containing samples and from 3% (ML005) to 21% (MLS003) for the magnetite-containing samples.

Using XRD it is possible to characterise the mineralogy, however differences in morphology are only detected by microscopy techniques. A complete analysis of the microstructure evolution and pore formation for all the samples in this study was given in a previous publication [35], which showed the strong relationship between chemical composition and porosity rather than the sintering conditions. Figure 2 shows the morphology of the HLS005 sample using SEM (Figure 2a) and HL001 using optical microscopy (Figure 2b). Different types of hematite were observed depending on the formation sequence. In this study, the following were observed: He1 (partially assimilated hematite, with a subhedral crystal shape); CF; γ-CFF, and pores. He2 (unreacted larger hematite), which benefits sinter strength [36], was also observed in a few samples.

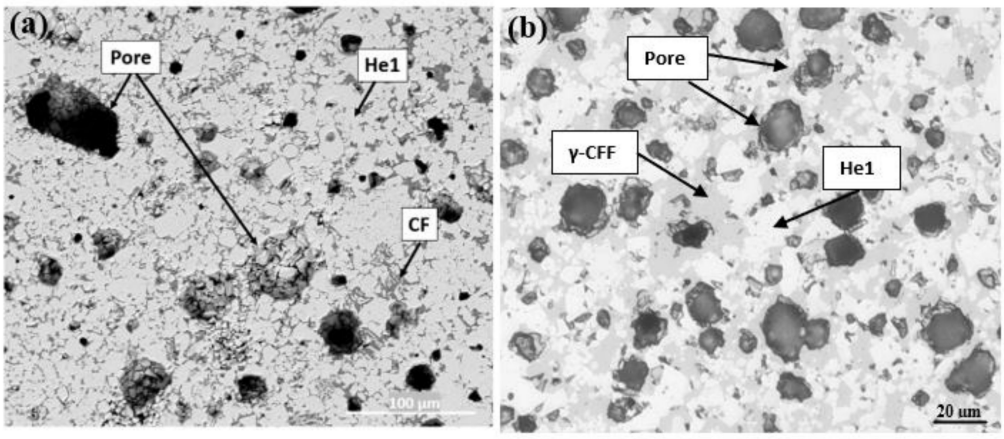


Figure 2. (**a**) BSE image of HLS005, (**b**) Optical microscopy image of HL001.

3.2. Effects of Chemistry on Maximum Temperature and Holding Time On
3.2.1. Strength

Figure 3a shows the TI for the samples when varying the maximum temperature, while Figure 3b shows the TI for the samples at different holding times. All the data are reported in Table 4. The variation in behaviours between the samples is a result of differences in mineralogy and structural factors. In general, the hematite-containing samples (H, HL and HLS) had higher strength compared to the magnetite-containing samples (M, ML

and MLS). The maximum strength development was achieved at highest T_{max} and t_{hold} of 1350 °C and 6 min, respectively. This agrees with previous studies [37–39], where the maximum strength also coincided with an increase in the overall melting of the sample. The samples had a slight increase in strength when fired for 2 to 6 min at 1300 °C than when fired for 4 min at different temperatures. Except for HLS001 and HLS005, none of the sinter analogues reached the minimum strength threshold (TI = 80) [17,20] for high-quality sinter.

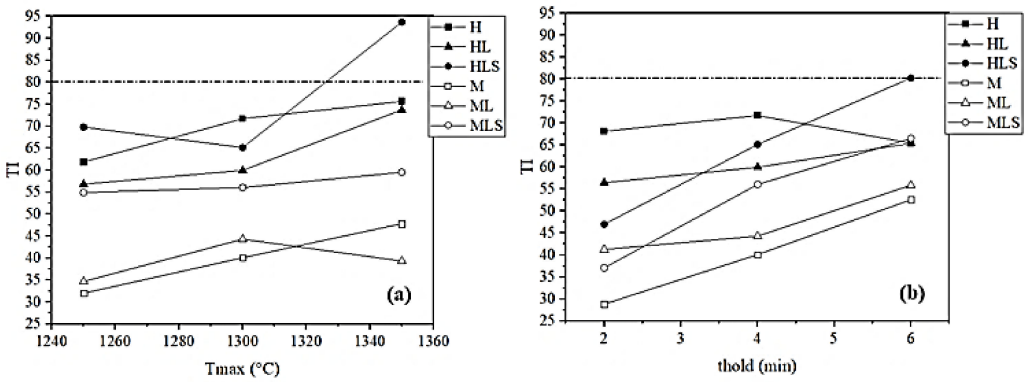


Figure 3. Laboratory tumble index data for all the thirty samples examined in this study. (**a**) TI vs T_{max} (t_{hold} = 4 min), (**b**) TI vs t_{hold} (T_{max} = 1300 °C). The dotted line at 80 indicates the strength threshold for high-quality sinter.

Table 4. Summary of the tumble index data for the various sample compositions in this study.

T_{max} (°C)	t_{hold} (min)	Tumble Index					
		H	HL	HLS	M	ML	MLS
1350	4	76	74	94	48	39	60
1300	4	72	60	65	40	44	56
1250	4	62	57	70	32	35	55
1300	2	68	56	47	29	41	37
1300	6	65	65	80	53	56	67

3.2.2. Porosity

Table 5 shows the MIP results for selected samples. The most porous sample was MLS003, with total porosity of 47%, followed by ML004, with 42%. On the other hand, the least porous sample was HL002, having only 0.66%. In general, total porosity decreased as the sintering maximum temperature (Figure 4a) and holding time increased (Figure 4b). This result agrees with the work of Harvey et al. [7], which also reported the inversely proportional relationship between porosity and temperature, caused by densification, which is a common process occurring in sintering where capillary pressure forces the melt into the pores, and an increased volume fraction of liquid. Wright [39] also reported porosity decreasing with higher holding times and temperatures. There was no evidence of microporosity in the samples, which could be expected as there is no presence of SFC and SFCA-like phases, which is responsible for retaining micropores in sinters [6].

3.3. Reducibility vs. Porosity

Reducibility indicates how easily the iron oxides lose oxygen when reacted with reducing gases. The reaction between Fe_2O_3 and CO generates FeO and releases CO_2, causing some shrinkage in the samples. Therefore, the weight loss of the sample after reduction is a strong indication of the reducibility of a sample. Figure 5 shows (a) the weight loss for all the samples in this study and also two industrial sinters (IS1 and IS2), after reduction under CO atmosphere at 950 °C for 150 min; and (b) the total porosity for selected samples using MIP.

Table 5. MIP results for selected samples in this study.

Samples	Sintering Conditions (T_{max}, t_{hold})	Total Porosity (%)
H001	1350 °C, 4 min	6.72
ML001		9.91
HL002	1300 °C, 4 min	0.66
HLS002		17.3
ML002		13.5
ML003	1250 °C, 4 min	22.3
MLS003		47.1
HLS004	1300 °C, 2 min	17.0
ML004		42.4
HLS005	1300 °C, 6 min	11.4
M005		5.98
ML005		6.50

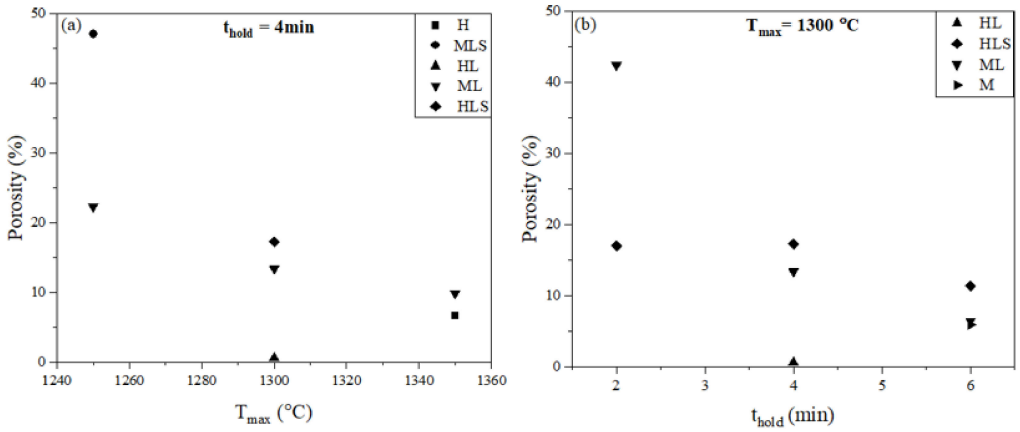


Figure 4. Porosity (%) measured by MIP. (**a**) Porosity vs T_{max} and (**b**) Porosity vs t_{hold}.

In general, the hematite-containing samples had higher reducibility than magnetite-containing samples for most of the sintering conditions. The lowest weight loss (<11.5%) was recorded in the MXX001 series of samples where the magnetite-containing samples fired at the highest temperature 1350 °C for 4 min. However, when the same composition samples were fired at lower temperatures and for shorter times (i.e., 1300 °C for 2 min, MXX004 series), they showed the highest weight loss (16 to 18%), indicating the highest reducibility among all the magnetite-containing samples. This could be explained by the considerable difference in porosity (from 10 to 42%), as there was no significant change in the mineralogy of those samples. The same phenomenon was observed for the MLS003 and MLS005 samples. The overall trend was an increase in reducibility with a decrease in T_{max} and t_{hold}, which confirms what was observed by Harvey et al., (2019), where over-sintering led to poor reducibility of the sinter analogues.

Most (80%) of the sinter analogue samples had a similar or higher reducibility than both industrial sinters even though the latter contained high contents of porous SFCA phases (Table 6). This provides strong evidence that sinter structure might play a more relevant role in the sinter reducibility than mineralogy. Figure 6 shows the strong relationship between the weight loss and porosity of the samples. In general, hematite and magnetite-containing samples behaved similarly, both increasing reducibility proportionally with porosity. Hematite-containing samples had higher reducibility than industrial sinter notwithstanding the lower porosities in the hematite-bearing samples. Perhaps the most interesting aspect is that results show that it is possible to obtain a very reducible magnetite-containing sample simply by manipulating the porosity through changing the

sintering conditions and chemistry (basicity and silica). A similar conclusion was reached by Purohit et al. [9], who identified that the generation of a $CaFe_3O_5$ (CWF) phase formed in lime-magnetite pellets under controlled conditions could generate a strong, porous, highly reducible sinter.

After reduction under a CO/N_2 atmosphere at 950 °C, the surface of the samples was visibly modified. Figure 7 shows reflected light images of polished cross-sections of the XXX003 series of samples (sintered at 1250 °C for 4 min) before and after reduction. QXRD results for the reduced samples show high levels of FeO and α-Fe, and smaller amounts of Fe_3O_4, Fe_2O_3 and other phases.

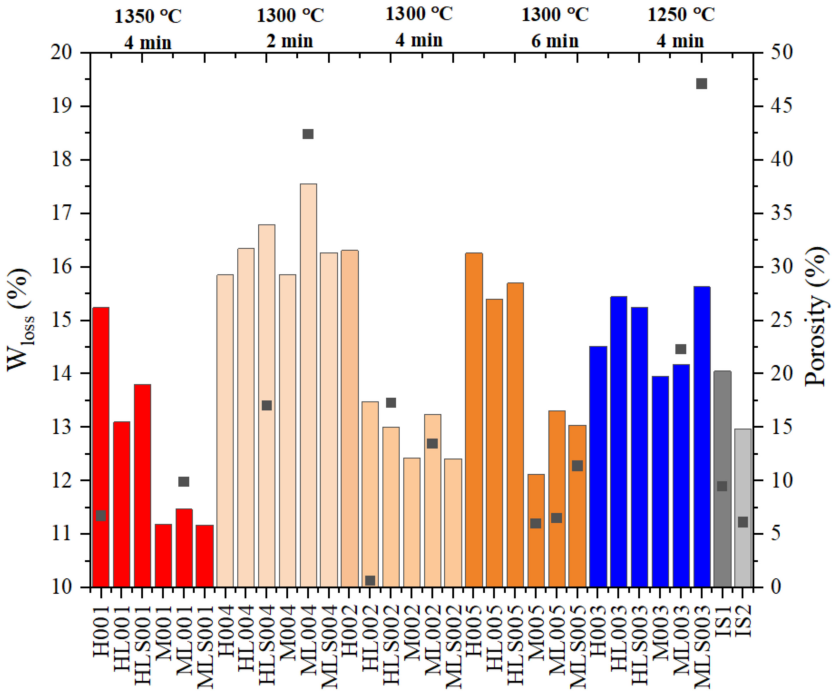


Figure 5. Weight loss (%) and porosity (%) (square dots) of sinter analogues and industrial samples.

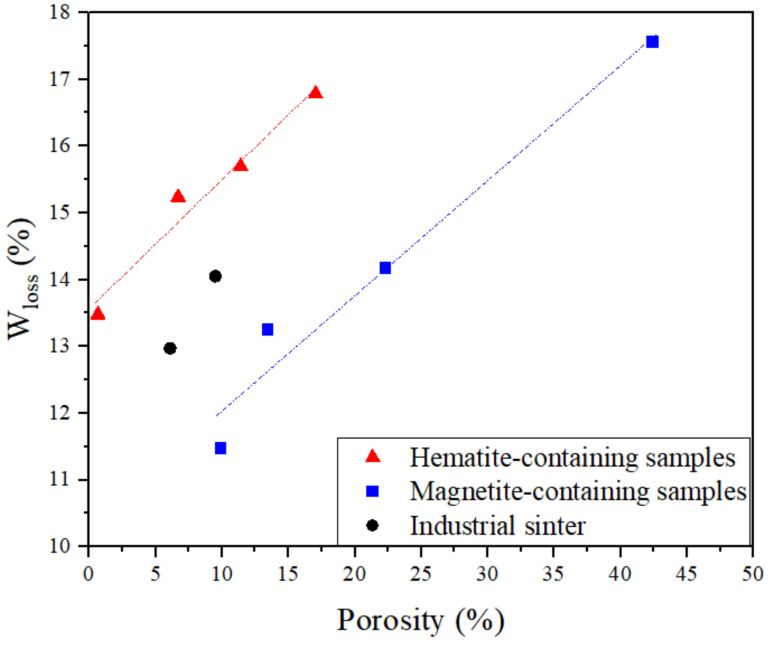


Figure 6. Relation between weight loss (%) and porosity (%).

Table 6. Crystalline phase concentration (relative wt%) for the pre-reduction industrial sinters.

	Total Hematite	Total Magnetite	Total SFCA ˆ	Others	Porosity (%)
IS1	26.9	16.3	40.9	15.9	9.52
IS2	28.4	18.0	33.5	20.1	6.10

ˆ note that only SFCA phase (not SFCA-I) was identified in these sinters.

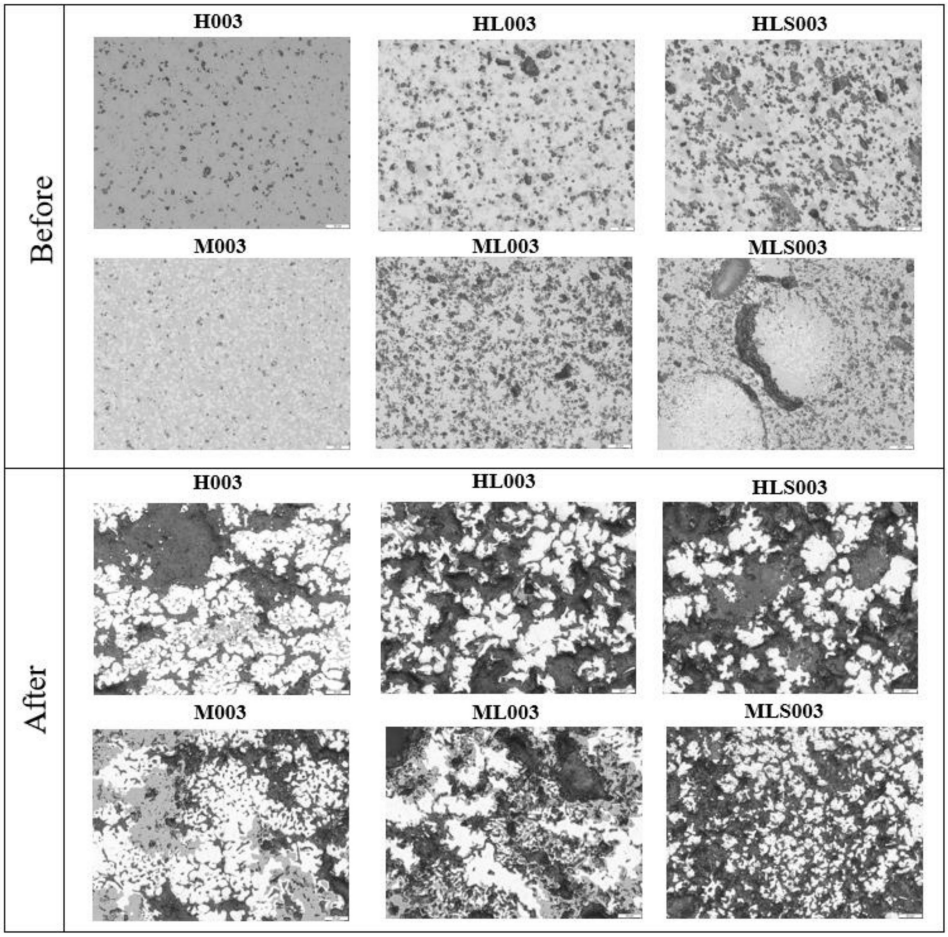


Figure 7. Reflected light micrographs of the XXX003 samples (1250 °C, 4 min) before and after reduction under a CO/N_2 atmosphere at 950 °C for 150 min. The after-reduction samples are dominated by the presence of metallic iron as indicated by the small, bright phase throughout the samples.

3.4. Porosity vs. Strength

The relation between porosity and strength has been investigated previously [39–41]. The general consensus is that porosity decreases strength as the pore channels act as a natural source of fractures as the stress increases due to the reduction in available area. Figure 8 shows the relation between TI and total porosity for the selected samples. The hematite-containing samples achieved the higher strength when porosity was around 11.4%, but strength quickly deteriorated for more porous samples. Interestingly, the magnetite-containing samples behaved completely differently. Their strength deteriorated rapidly with increasing porosity, reaching the lowest strength at 22.3% porosity, but improving strength again at higher porosity levels (>22%).

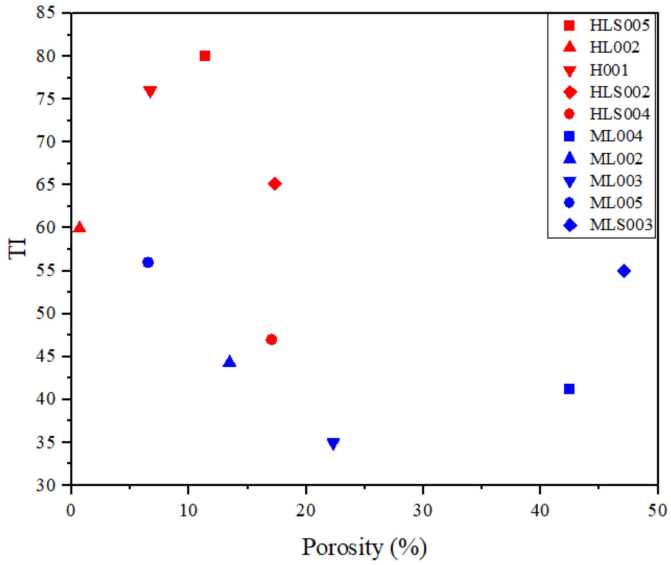


Figure 8. Relation between tumble index (TI) and porosity (%). Hematite-containing samples in red and magnetite-containing samples in blue.

4. Conclusions

Iron ore sinter analogues from the Fe_2O_3-(Fe_3O_4)-CaO-SiO_2 (FCS) ternary system were sintered in controlled laboratory tests where maximum temperature and holding time were varied, and the influence at these variables on their mineralogy, porosity, reducibility and strength were evaluated. It can be concluded that:

(1) The formation of calcium ferrites was mostly affected by the sintering conditions rather than the basicity for the hematite-containing samples. The same trend was not observed for the magnetite-containing samples.
(2) The reducibility of the sinter analogues was found to be strongly related to porosity, as expected. The reducibility of the magnetite-containing samples was relatively insensitive to mineralogy.
(3) Most (around 80%) of the sinter analogues samples had similar or higher reducibility than the two industrial sinters (with high contents of SFCA phase) analysed in this study. This is evidence that sinter porosity might play a more relevant role in sinter reducibility than does mineralogy.
(4) Pore formation can be manipulated by changing the sintering conditions (lower T_{max} and shorter t_{hold}) and chemical composition (adding lime and silica to the samples).
(5) The magnetite-containing samples (MXX003 and MXX004 series) had similar reducibilities to hematite-containing samples (HXX003 and HXX004 series), suggesting that magnetite sinters could be used in the blast furnace.

It is recommended that in future work on sinter quality parameters a broader range of values (such as temperature, holding time and basicity) be analysed for a more detailed understanding of their influence on porosity and strength. It is also recommended that the compositional range be expanded to include the effects of alumina, which would be more in line with industrial sinters.

Author Contributions: Conceptualization, G.B., M.I.P. and I.R.I.; Methodology, I.R.I., G.B., M.I.P. and N.A.S.W.; Validation, I.R.I., G.B., M.I.P., M.A.R., W.J.R. and N.A.S.W.; Formal Analysis, I.R.I., G.B., M.I.P., M.A.R. and W.J.R.; Investigation, I.R.I., G.B., M.I.P., M.A.R., W.J.R. and N.A.S.W.; Resources, G.B., M.I.P. and M.A.R.; Data Curation, I.R.I. and N.A.S.W.; Writing—Original Draft Preparation, I.R.I.; Writing—Review & Editing, I.R.I., G.B., M.I.P., M.A.R., W.J.R. and N.A.S.W.; Visualization, I.R.I., G.B., M.I.P., M.A.R. and W.J.R.; Supervision, G.B., M.I.P., M.A.R. and W.J.R.; Project Administration, G.B.; Funding Acquisition, G.B. and M.I.P. All authors have read and agreed to the published version of the manuscript.

Funding: This research received no external funding.

Data Availability Statement: Not applicable.

Acknowledgments: The authors acknowledge the Swinburne University of Technology and the Commonwealth Scientific and Industrial Research Organisation (CSIRO) for providing financial support for this research through the Australian Government Research Training Program (RTP) Scholarship and a CSIRO Ph.D. Top-up Scholarship, respectively. The authors also thank Natalie Ware (Mineral Resources, Pullenvale) for carrying out tumble index testing and Rodrigo Gomez-Camacho (CSIRO Mineral Resources, Waite) for XRD sample preparation.

Conflicts of Interest: The authors declare no conflict of interest.

References

1. Lu, L.; Ishiyama, O. Iron ore sintering. In *Iron Ore: Mineralogy, Processing and Environmental Sustainability*; Lu, L., Ed.; Elsevier: Amsterdam, The Netherlands, 2015; pp. 395–433.
2. Bhagat, R.P. Sintering Fundamentals. In *Agglomeration of Iron Ores*; CRC Press: Boca Raton, FA, USA, 2019; pp. 117–184.
3. Biswas, A.K. Raw materials and their properties. In *Principle of Blast Furnace Ironmaking, Theory and Practice*; Cootha Publishing House: Brisbane, Australia, 1981; pp. 188–261.
4. Pownceby, M.I.; Clout, J.M.F. Importance of fine ore chemical composition and high temperature phase relations: Applications to iron ore sintering and pelletising. *Trans. Inst. Min. Metall. Sect. C Miner. Process. Extr. Metall.* **2003**, *112*, 44–51. [CrossRef]
5. Harvey, T.; O'Dea, D.; Evans, G.M.; Honeyands, T. Influence of sintering conditions on the reducibility of iron ore sinter analogues. In Proceedings of the Iron Ore Conference, Perth, WA, Australia, 22–24 July 2019; pp. 862–871.
6. Bristow, N.J.; Waters, A.G. Role of SFCA in promoting high temperature reduction properties of iron ore sinters. *Trans. Inst. Min. Metall. Sect. C Miner Process. Extr. Metall.* **1991**, *100*, 1–10.
7. Harvey, T.; Honeyands, T.; O'Dea, D.; Evans, G. Study of sinter strength and pore structure development using analogue tests. *ISIJ Int.* **2019**, *60*, 73–83. [CrossRef]
8. Shatokha, V.; Korobeynikov, I.; Maire, E.; Grémillard, L.; Adrien, J. Iron ore sinter porosity characterisation with application of 3D X-ray tomography. *Ironmak. Steelmak.* **2010**, *37*, 313–319. [CrossRef]
9. Purohit, S. Alternative Processing Routes for Magnetite Ores. Ph.D. Thesis, Swinburne University of Technology, Melbourne, Australia, 2019.
10. Pownceby, M.I.; Patrick, T.R.C. Stability of SFC (silico-ferrite of calcium): Solid solution limits, thermal stability and selected phase relationships within the Fe_2O_3-CaO-SiO_2 (FCS) system. *Eur. J. Mineral.* **2000**, *12*, 455–468. [CrossRef]
11. Webster, N.A.S.; Pownceby, M.I. In-situ X-ray diffraction analysis of phase formation during heating of silico-ferrite of calcium (SFC) compositions. *ISIJ Int.* **2022**, *62*, 1624–1628. [CrossRef]
12. Murao, R.; Kimura, M. Investigation on reaction schemes of iron ore sintering process by high temperature in-situ X-ray diffraction and micro-texture observation. *Nippon Steel Sumitomo Met. Tech. Rep.* **2018**, *118*, 59–64.
13. Bhagat, R.P.; Chattoraj, U.S.; Goswami, M.C.; Singh, D.P.; Sil, S.K. Effect of size parameters of mix ingredients on the porosity and reduction characteristics of sinter. *Steel Res. Int.* **2007**, *78*, 451–454. [CrossRef]
14. Hsieh, L.H.; Whiteman, J.A. Effect of oxygen potential on mineral formation in lime-fluxed iron ore sinter. *ISIJ Int.* **1989**, *29*, 625–634. [CrossRef]
15. Harvey, T. Influence of Mineralogy and Pore Structure on the Reducibility and Strength of Iron Ore Sinter. Ph.D. Thesis, University of Newcastle, Newcastle, Australia, 2020.
16. Clout, J.M.F. Formation of key iron ore sinter phases from Hamersley fines: Implications for ultra fines chemistry and sinter formation. *CSIRO* **1994**, 107–115.
17. Ware, N.; Manuel, J.R.; Raynlyn, T.; Lu, L. Melting behaviour of hematite and goethite fine ores and its potential impact on sinter quality. In Proceedings of the Iron Ore Conference, Perth, WA, Australia, 12–14 August 2013; pp. 485–486.
18. Ware, N.; Manuel, J. Fundamental nucleus assimilation behaviour of haematite and goethite containing ores in iron ore sintering. *Trans. Inst. Min. Metall. Sect. C Miner. Process. Extr. Metall.* **2016**, *125*, 149–155. [CrossRef]
19. Clout, J.M.F.; Manuel, J.R. Fundamental investigations of differences in bonding mechanisms in iron ore sinter formed from magnetite concentrates and hematite ores. *Powder Technol.* **2003**, *130*, 393–399. [CrossRef]
20. Pownceby, M.I.; Webster, N.A.S.; Manuel, J.R.; Ware, N. The influence of ore composition on sinter phase mineralogy and strength. *Trans. Inst. Min. Metall. Sect. C Miner. Process. Extr. Metall.* **2016**, *125*, 140–148. [CrossRef]
21. Purohit, S.; Brooks, G.; Rhamdhani, M.A.; Pownceby, M.; Webster, N.A.S. Alternative route for magnetite processing for lower carbon footprint iron-making through lime-magnetite pellets containing $CaFe_3O_5$. *Ironmak. Steelmak.* **2020**, *47*, 674–685. [CrossRef]
22. *ISO 7215:2015*; Iron Ores for Blast Furnace Feedstocks—Determination of the Reducibility by the Final Degree of Reduction Index. International Organization for Standardization: Geneva, Switzerland, 2015.
23. Klobes, P.; Munro, R.G. Porosity and Specific Surface Area Measurements for Solid Materials. 2006. Available online: https://tsapps.nist.gov/publication/get_pdf.cfm?pub_id=854263 (accessed on 27 September 2022).
24. Espinal, L. Porosity and Its Measurement. *Charact. Mater.* **2002**, 1–10. [CrossRef]

25. Rouquerol, J.; Avnir, D.; Fairbridge, C.W.; Everett, D.H.; Haynes, J.M.; Pernicone, N.; Ramsay, J.D.F.; Sing, K.S.W.; Unger, K.K. Recommendations for the characterization of porous solids (Technical Report). *Pure Appl. Chem.* **1994**, *66*, 1739–1758. [CrossRef]
26. Pownceby, M.I.; Clout, J.M.F. Phase relations in the Fe-rich part of the system Fe_2O_3 (– Fe_3O_4)– CaO – SiO_2 at 1240–1300 °C and oxygen partial pressure of 5×10^{-3} atm: Implications for iron ore sinter. *Miner. Process. Extr. Metall.* **2013**, *109*, 36–48. [CrossRef]
27. Pownceby, M.I.; Clout, J.M.F.; Fisher-White, M.J. Phase equilibria for the Fe_2O_3-rich part of the system Fe_2O_3-CaO-SiO_2 in air at 1240–1300 degrees C. *Trans. Inst. Min. Metall. Sect. C Miner. Process. Extr. Metall.* **1998**, *107*, 1–10.
28. Patrick, T.R.C.; Pownceby, M.I. stability of silico-ferrite of calcium and aluminum (SFCA) in air—Solid solution limits between 1240 °C and 1390 °C and phase relationships within the Fe_2O_3-CaO-Al_2O_3-SiO_2 (FCAS) system. *Metall. Mater. Trans. B* **2002**, *33*, 79–89. [CrossRef]
29. Ding, X.; Guo, X. The formation process of silico-ferrite of calcium (SFC) from binary calcium ferrite. *Metall. Mater. Trans. B* **2014**, *45B*, 1221–1231. [CrossRef]
30. Scarlett, N.V.Y.; Pownceby, M.I.; Madsen, I.C.; Christensen, A.N. Reaction sequences in the formation of silico-ferrites of calcium and aluminum in iron ore sinter. *Process Metall. Mater. Process. Sci.* **2004**, *35*, 929–936. [CrossRef]
31. Karpinskii, O.G.; Arakcheeva, A.V. Crystal structure of ternary hexagonal ferrite phase of $Ca_{3.565}$ $Fe_{0.06}$ $Fe_{14.25}O_{25}$. *Sov. Phys. Dokl.* **1985**, *20*, 439.
32. Arakcheeva, A.V.; Karpinskii, O.G. Crystal structure of hexagonal ferrite, $Ca_{2,95}Fe_{14,85}O_{25}$. *Dokl. Akad. Nauk SSSR* **1983**, *273*, 1127–1129.
33. Arakcheeva, A.V.; Karpinskii, O.G. Crystal structure of the ternary hexagonal Ca ferrite $Ca_{3.0}Fe_{14.82}O_{25}$. *Sov. Phys. Crystallogr.* **1987**, *32*, 31–32.
34. Murakami, T.; Wakabayashi, H.; Maruoka, D.; Kasai, E. Effect of hydrogen concentration in reducing gas on the changes in mineral phases during reduction of iron ore sinter. *ISIJ Int.* **2020**, *60*, 2678–2685. [CrossRef]
35. Ignacio, I.R.; Brooks, G.; Pownceby, M.I.; Rhamdhani, M.A.; Rankin, W.J. Porosity in iron ore sintering. In Proceedings of the Iron Steel Technology Conference, Pittsburgh, PA, USA, 16–18 May 2022; pp. 1821–1830.
36. Hapugoda, S.; Lu, L.; Donskoi, E.; Manuel, J. Mineralogical quantification of iron ore sinter. *Miner. Process. Extr. Metall.* **2016**, *125*, 156–164. [CrossRef]
37. Dehghan-Manshadi, A.; Manuel, J.; Hapugoda, S.; Ware, N. Sintering characteristics of titanium containing iron ores. *ISIJ Int.* **2014**, *54*, 2189–2195. [CrossRef]
38. Pownceby, M.I.; Webster, N.A.S.; Manuel, J.; Ware, N. Iron ore geometallurgy—Examining the influence of ore composition on sinter phase mineralogy and sinter strength. In Proceedings of the Iron Ore Conference, Perth, WA, Australia, 10–11 March 2015; pp. 579–586.
39. Wright, J.K. The effect of firing conditions on the strength of hematite compacts. *Powder Technol.* **1976**, *14*, 103–113. [CrossRef]
40. Wynnyckyj, J.R.; Fahidy, T.Z. Solid state sintering in the induration of iron ore pellets. *Met. Trans.* **1974**, *5*, 991–1000. [CrossRef]
41. Wright, J.K.; Tyler, R.J. Pore structures of sintered and metallized iron oxide compacts. *Powder Technol.* **1979**, *24*, 49–55. [CrossRef]